photonics

MDPI

Communication

Nonzero-Order Resonances in Single-Beam Spin-Exchange Relaxation-Free Magnetometers

Kun Wang [1,2], Kaixuan Zhang [2,*], Nuozhou Xu [1,2], Yifan Yan [1,2], Xiaoyu Li [1,2] and Binquan Zhou [1,2]

[1] Key Laboratory of Ultra-Weak Magnetic Field Measurement Technology, Ministry of Education, School of Instrumentation and Optoelectronic Engineering, Beihang University, Beijing 100191, China
[2] Zhejiang Provincial Key Laboratory of Ultra-Weak Magnetic-Field Space and Applied Technology, Hangzhou Innovation Institute, Beihang University, Hangzhou 310051, China
* Correspondence: zhangkx@shanghaitech.edu.cn

Abstract: Zero-field optically pumped magnetometers operating in the spin-exchange relaxation-free (SERF) regime have been extensively studied, and usually depend on zeroth-order parametric resonance to measure the magnetic field. However, the studies conducted on this topic lack thorough analyses and in-depth discussion of nonzero-order magnetic resonances in single-beam SERF magnetometers. In this paper, we analyzed the nonzero-order resonance, especially the first-order resonance, based on a single-beam SERF magnetometer, and discussed its various applications. A comprehensive theoretical analysis and experiments were conducted with respect to multiple functions, including nonzero finite magnetic field measurements, spin polarization measurement, and in situ coil constant calibration. The results showed that first-order resonance can be utilized for nonzerofinite magnetic field measurements, and the spin polarization of alkali-metal atoms can be determined by measuring the slowing-down factor using the resonance condition. Furthermore, acquiring the first-order resonance point at an equivalent zero pump light power through fitting offers an approach for quick and precise in situ coil constant calibration. This study contributes to the applications of SERF magnetometers in nonzero finite magnetic fields.

Keywords: SERF magnetometers; parametric resonances; slowing-down factor; spin polarization; coil constant calibration

Citation: Wang, K.; Zhang, K.; Xu, N.; Yan, Y.; Li, X.; Zhou, B. Nonzero-Order Resonances in Single-Beam Spin-Exchange Relaxation-Free Magnetometers. *Photonics* **2023**, *10*, 458. https://doi.org/10.3390/photonics10040458

Received: 9 March 2023
Revised: 7 April 2023
Accepted: 12 April 2023
Published: 15 April 2023

1. Introduction

Optically pumped magnetometers (OPMs) have attracted considerable attention owing to their ultra-high sensitivity, flexible positioning, and cryogenic-free working conditions, and they provide superior advantages over traditional superconducting quantum interference devices [1–3]. They are increasingly used in fundamental physics [4,5], geophysical measurements [6,7], and magnetic imaging of the human body [8,9]. In particular, OPMs operating in the spin-exchange relaxation-free (SERF) regime have undergone rapid development [10,11]. Thanks to their convenient miniaturization, SERF magnetometers with single-beam configuration, employing power detection of transmitted circularly polarized pump light to measure the magnetic field, are the most commonly applied scheme [12–15], and their operation relies on transverse magnetic field modulation and zeroth-order parametric resonance.

The parametric resonance response theory of light-pumped atoms in a modulated magnetic field was dissertated by Cohen-Tannoudji et al. in 1970 [16] and was demonstrated by Slocum et al. in 1973 using a ^{4}He magnetometer [17]; however, they mainly focused on the zeroth-order resonance. Nevertheless, there are still only a few studies on the first-order or higher-order resonances. For instance, Xiao et al. proposed that the first-order resonance of a SERF magnetometer could be employed to calibrate coil constants and simultaneously showed the possibility of measuring a magnetic field under a large field background [18]. For other types of magnetometers, Eklund [19] and Chen et al. [20]

employed the resonance order of rubidium magnetization and discussed its application in nuclear magnetic resonance. Jiang et al. developed a rubidium atomic magnetometer that satisfies the first-order resonance to study the heater-induced longitudinal magnetic field [21]. Yang et al. proposed a novel plan for magnetic sensing based on multi-order resonance utilizing an M_x magnetometer, and the measurement sensitivity was below 3 pT/Hz$^{1/2}$ [22]. However, these studies lack comprehensive analyses and detailed discussion of nonzero-order magnetic resonances in single-beam SERF magnetometers; therefore, a comprehensive study on this topic is still desirable.

In this study, we analyzed several phenomena with respect to the nonzero-order resonances of single-beam SERF magnetometers and discussed their applications, including spin polarization measurement and coil constant calibration. We conducted a theoretical analysis, numerical simulation, and experiments to study the parametric resonance phenomena and their applications. First, a nonzero finite magnetic field was measured. A finite magnetic field was acquired by detecting the resonant frequency in combination with the resonance condition. Second, the spin polarization of alkali-metal atoms was measured by measuring the slowing-down factor $q(P)$ based on the resonance condition. Finally, the first-order resonance point at the equivalent zero light power with a definitive known $q(P)$ was determined by fitting; this offered a method to calibrate the coil constants rapidly and precisely. Moreover, the sensitivity of the magnetic field measurement reached 54 fT/Hz$^{1/2}$.

2. Principles

OPMs are employed to measure the magnetic field by detecting the time evolution of atomic spin polarization created by optical pumping. When the spin-exchange rate is significantly higher than the Larmor precession frequency, the Bloch equation derived from the density matrix equations can be adopted to describe the behavior of the atomic spin polarization vector **P** [23] as follows:

$$\frac{d\mathbf{P}}{dt} = \frac{1}{q(P)}\left[\gamma^e \mathbf{B} \times \mathbf{P} + R_{\mathrm{op}}(s\hat{z} - \mathbf{P}) - R_{\mathrm{rel}}\mathbf{P}\right] \tag{1}$$

where P is the magnitude of the atomic spin polarization vector, $\mathbf{P} = \left[P_x, P_y, P_z\right]^{\boldsymbol{T}}$; and $q(P)$ is the nuclear slowing-down factor as a function of P [24]. In particular, for ^{87}Rb atoms ($I = 3/2$) the expression of $q(P)$ is given as

$$q(P) = \frac{6 + 2P^2}{1 + P^2} \tag{2}$$

which indicates that the amplitude of spin polarization can be obtained by measuring $q(P)$. In addition, $\gamma^e \approx 2\pi \times 28$ Hz/nT is the gyromagnetic ratio of the electron, **B** is the magnetic field vector expressed as $\mathbf{B} = \left[B_x, B_y, B_z\right]^T$, R_{op} is the optical pumping rate, R_{rel} is the spin-relaxation rate, and s is the degree of circular polarization of the pump light whose direction propagates along the z-axis; for circularly polarized light, this is s = $\pm$1.

Specifically, for single-beam OPMs, the transmitted light intensity of a circularly polarized laser beam which only reflects the longitudinal polarization P_z can act as a magnetic field information medium [25–27]. The relationship between the output of the magnetometer R_{out} and P_z is given as [25]

$$R_{out} = R_0 \cdot \exp[-\mathrm{OD}(\nu)(1 - P_z)] \tag{3}$$

where R_0 is the original signal before the vapor cell; $\mathrm{OD}(\nu) = n_\nu L\sigma(\nu)$ is the optical depth of the vapor cell; n_ν is the number density of the alkali-metal vapor; $\sigma(\nu)$ is the absorption cross-section as a function of light frequency ν; and L is the length of the vapor cell. Thus, the response of P_z to a magnetic field is the subject of concern. In single-beam SERF magnetometers, a bias magnetic field B_{x0} and a modulation field $B_m\cos(\omega t)$ were applied

along the x-axis, as shown in Figure 1a. After magnetic compensation, the magnetic field along the three axes was described as $\mathbf{B} = [B_{x0} + B_m\cos(\omega t), 0, 0]^T$. From Equation (1), we know that $P_x(t)$ approaches zero, and $\mathbf{P}$ oscillates and evolves only in the y-z plane. Therefore, we define polarization as $P_+ = P_z + iP_y$, which follows the evolution

$$\frac{dP_+}{dt} = \frac{1}{q(P)}\{-i\gamma^e[B_{x0} + B_m\cos(\omega t)]P_+ - (R_{\mathrm{op}} + R_{\mathrm{rel}})\mathrm{P}_+ + R_{\mathrm{op}}\} \tag{4}$$

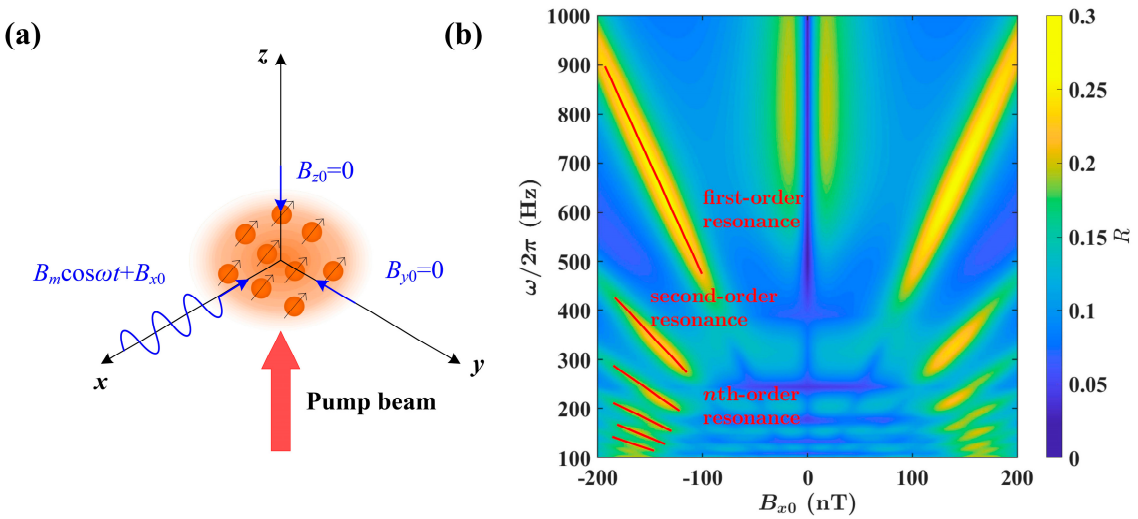

Figure 1. (**a**) Schematic of our single-beam SERF magnetometer with the modulated magnetic field along the x-axis. (**b**) Simulation results of the magnetometer response R under different $\omega/2\pi$ and B_{x0}, with $B_m = 200$ nT.

After employing the Jacobi-Anger expansion and mathematical derivation, the analytical solution to P_z can be obtained as [16,17,19]

$$\begin{aligned} P_z(t) \quad = & \sum_{n=-\infty}^{+\infty}\sum_{k=-\infty}^{+\infty} \frac{R_{\mathrm{op}}J_n(u)J_{n+k}(u)}{(R_{\mathrm{op}}+R_{\mathrm{rel}})^2+(\gamma^e B_{x0}+nq\omega)^2}\left[(R_{\mathrm{op}} + R_{\mathrm{rel}})\cos(k\omega t)\right. \\ & \left. + (\gamma^e B_{x0} + nq\omega)\sin(k\omega t)\right] \end{aligned} \tag{5}$$

where $J_n(u)$ is the nth-order Bessel function of the first kind; and $u = \gamma^e B_m/(q\omega)$ is the modulation index. Here, n denotes the resonance order, with each order appearing at the magnetic field offset satisfying $\gamma^e B_{x0} + nq\omega = 0$.

To eliminate low-frequency 1/f noise, the lock-in detection system for the first harmonic ω, the dominant term of the spectrum, was employed. The longitudinal polarization embodied in the demodulated signal is $P_{z-de}(t)$, which is expressed as follows:

$$\begin{aligned} P_{z-de}(t) = & \sum_{n=-\infty}^{+\infty} \frac{R_{\mathrm{op}}J_n(u)}{(R_{\mathrm{op}}+R_{\mathrm{rel}})^2+(\gamma^e B_{x0}+nq\omega)^2}\left\{(R_{\mathrm{op}} + R_{\mathrm{rel}})[J_{n+1}(u) + J_{n-1}(u)]\cos(\omega t)\right. \\ & \left. + (\gamma^e B_{x0} + nq\omega)[J_{n+1}(u) - J_{n-1}(u)]\sin(\omega t)\right\} \end{aligned} \tag{6}$$

The demodulated in-phase component X_n and out-of-phase component Y_n for the nth-order resonance are

$$X_n = J_n(u)[J_{n+1}(u) + J_{n-1}(u)]\frac{R_{\mathrm{op}}(R_{\mathrm{op}} + R_{\mathrm{rel}})}{(R_{\mathrm{op}} + R_{\mathrm{rel}})^2 + (\gamma^e B_{x0} + nq\omega)^2} \tag{7}$$

$$Y_n = J_n(u)[J_{n+1}(u) - J_{n-1}(u)]\frac{R_{\mathrm{op}}(\gamma^e B_{x0} + nq\omega)}{(R_{\mathrm{op}} + R_{\mathrm{rel}})^2 + (\gamma^e B_{x0} + nq\omega)^2} \tag{8}$$

The amplitude component R_n depends both on X_n and Y_n:

$$R_n = \sqrt{X_n^2 + Y_n^2} \tag{9}$$

Here, X_n and Y_n are closely related to the phase of the demodulation process, and the phase varies when the sweeping magnetic field is offset. Consequently, R_n was selected as observable in our experiment. The Y_n component presented a dispersion relation with B_{x0} near the nth resonance point $B_{xn} = -nq\omega/\gamma^e$, which can be utilized for magnetic field measurement. The total in-phase component X, total out-of-phase component Y, and total amplitude component R are expressed as $X = \sum_{n=-\infty}^{n=+\infty} X_n$, $Y = \sum_{n=-\infty}^{n=+\infty} Y_n$, and $R = \sum_{n=-\infty}^{n=+\infty} R_n$, respectively.

The analysis of each order of resonance was based on the response amplitude R of the magnetometer, owing to its insensitivity to the demodulation phase. We performed a simulation to calculate the magnetometer response R under different $\omega/2\pi$ and B_{x0}, with typical experimental parameters of $R_{\mathrm{op}} = R_{\mathrm{rel}} = 250\ \mathrm{s}^{-1}$ and $B_m = 200$ nT. The simulation covered a span range of $\omega/2\pi$ from 100 Hz to 1000 Hz and a span range of B_{x0} from -200 nT to 200 nT, as depicted in Figure 1b. From the simulation, we found that the resonance point B_{x0} of each order was linear to $\omega/2\pi$ under resonance conditions, whereas the interval between each order increased when $\omega/2\pi$ grew. Furthermore, the attenuation of the modulation index u, corresponding to the growth of $\frac{\omega}{2\pi}$, results in the gradual dominance of the lower-order resonance, indicating that u must be controlled in the appropriate range to maintain the predominance of the first-order resonance. In other words, the higher-order resonance response of the magnetometer ($n > 1$) only emerges markedly with lower $\omega/2\pi$ (<350 Hz, shown in Figure 1b), which restricts the performance of the lock-in system and further limits the sensitivity of measurement. Moreover, Figure 1b shows that the higher-order resonance response ($n > 1$) appears at an absolute value of magnetic offset larger than 100 nT, which can induce strong relaxation of alkali atoms. Hence, in this study, our attention was mostly paid to the first-order resonance response.

In addition, by focusing on the amplitude of the demodulated signal at each resonance order, we found that if $n \neq 0$ then $Y_n = 0$. By contrast, when $n = 0$, $X_n = 0$. Consequently, the demodulated signal at the nth-order resonance is given as

$$R_n^{\mathrm{res}} = \begin{cases} \frac{2J_0(u)J_1(u)R_{\mathrm{op}}\gamma^e B_{x0}}{\left(R_{\mathrm{op}}+R_{\mathrm{rel}}\right)^2+\left(\gamma^e B_{x0}\right)^2} = 0 & n = 0 \\ \frac{2nJ_n^2(u)}{u} \cdot \frac{R_{\mathrm{op}}}{R_{\mathrm{op}}+R_{\mathrm{rel}}} & n \neq 0 \end{cases} \tag{10}$$

and the linear region of R_n^{res} could be utilized to measure the low-frequency alternating magnetic field [22].

We revealed that the magnitude of spin polarization at the first-order resonance point is constant and time-independent. At the first-order resonance point, by substituting $n = 1$ ($n = -1$ is similar) and $\gamma^e B_{x0} + q\omega = 0$ conditions for the corresponding expressions in Equation (5), we obtain

$$\begin{aligned} P_z(t) &= \frac{R_{\mathrm{op}}J_1(u)}{R_{\mathrm{op}}+R_{\mathrm{rel}}} \sum_{k=-\infty}^{+\infty} J_{k+1}(u)\cos(k\omega t) \\ &= \frac{R_{\mathrm{op}}J_1(u)}{R_{\mathrm{op}}+R_{\mathrm{rel}}} \{\sin(\omega t)\sin[u\sin(\omega t)] + \cos(\omega t)\cos[u\sin(\omega t)]\} \end{aligned} \tag{11}$$

Similar equations can be derived for $P_y(t)$ utilizing the same method as

$$\begin{aligned} P_y(t) &= \frac{R_{\mathrm{op}}J_1(u)}{R_{\mathrm{op}}+R_{\mathrm{rel}}} \sum_{k=-\infty}^{+\infty} J_{k+1}(u)\sin(k\omega t) \\ &= \frac{R_{\mathrm{op}}J_1(u)}{R_{\mathrm{op}}+R_{\mathrm{rel}}} \{\cos(\omega t)\sin[u\sin(\omega t)] - \sin(\omega t)\cos[u\sin(\omega t)]\} \end{aligned} \tag{12}$$

As $P_x(t)$ approaches zero, the amplitude of total spin polarization is given as

$$P = \sqrt{[P_z(t)]^2 + [P_y(t)]^2} = \frac{R_{\mathrm{op}} J_1(u)}{R_{\mathrm{op}} + R_{\mathrm{rel}}} \tag{13}$$

Here, we assumed that R_{op}, R_{rel}, and $J_1(u)$ are invariant during the experiment. The resulting stable magnitude of P can be applied to derive the fit function in the following Sections 4.2 and 4.3.

3. Experimental Setup and Procedure

The experimental setup for measuring the magnetic field, based on the first-order parametric resonances of our single-beam SERF magnetometer, is illustrated in Figure 2. A cubic vapor cell made of borosilicate glass, with an internal size of 8 mm × 8 mm × 8 mm, was filled with a droplet of ^{87}Rb and approximately 600 Torr N_2. The vapor cell was electrically heated to 433 K using an alternating current at 200 kHz.

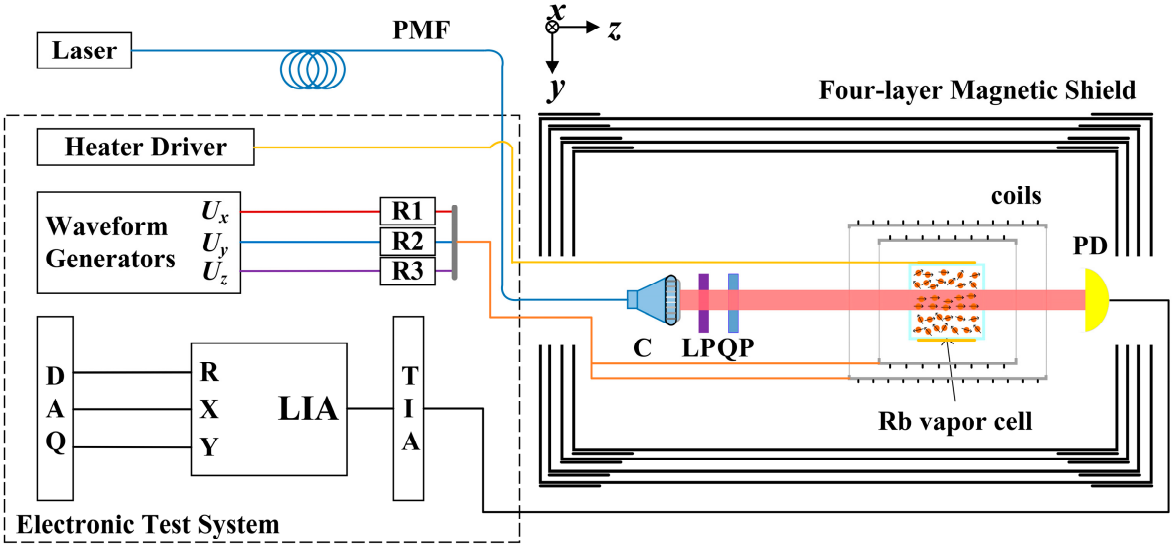

Figure 2. Experimental setup. PMF: polarization maintaining fiber; C: collimating lens; LP: linear polarizer; QP: quarter-wave plate; PD: photodiode; TIA: transimpedance amplifier; LIA: lock-in amplifiers; DAQ: data-acquisition; R1, R2, and R3: resistors.

The laser beam generated by a distributed-feedback laser was first transmitted to the OPM via a polarization-maintaining fiber, and then was transformed into circularly polarized light using a quarter-wave plate, which finally illuminated the vapor cell; this acts as both an optical pumping and probing light. The wavelength of the laser beam was set to approximately 794.98 nm, near the ^{87}Rb D1 line. The light transmitted through the vapor cell was sensed and converted into a current signal by the photodiode, then finally transformed into a voltage signal by the trans-impedance amplifier (PDA200C; Thorlabs, Newton, MA, USA).

The voltage signal was then sent to the electronic test system for signal processing. In the electronic system, a lock-in amplifier (MFLI; Zurich Instruments, Zürich, Switzerland) was used to demodulate the magnetometer signal. Finally, all signals were acquired using the data-acquisition system (PXIe-4464; National Instruments, Austin, TX, USA).

A four-layer μ-metal magnetic shield was utilized to ensure a near-zero magnetic field environment for the OPM. In addition, a group of triaxial coils inside the shield was adopted for further active magnetic field compensation and generation of modulated magnetic fields. The coil group comprised a nested saddle coil [28] for the radial magnetic field and a Lee-Whiting coil [29] for the axial magnetic field; these were both driven by waveform generators (33522B; Keysight, Santa Rosa, United States) via selected resistors.

The experiment primarily comprised three steps. First, we demonstrated the measurement of the non-zero finite magnetic field based on the first-order resonance of the magnetometer. The measurement of the non-zero finite field was realized by detecting the resonance frequency, according to $B_{\mathrm{un}} = nq(P)\omega/\gamma^e$. Second, spin polarization measurement was implemented by measuring the slowing-down factor, and this process was staged with different modulated magnetic field amplitudes. Finally, we performed a precise coil constant calibration by fitting the first-order resonance points under different pump light powers and acquiring the point at equivalent zero pump light powers.

4. Results and Discussions

4.1. Nonzero Finite Magnetic Field Measurement

In this subsection, a method for measuring the non-zero finite magnetic field based on the first-order resonance is proposed and demonstrated. The non-zero finite field was measured by detecting the resonant frequency. Before sweeping the modulated magnetic field frequency, we first swept the magnetic field offset to acquire the slowing-down factor q at each first-order resonance point. Specifically, the magnetic field offset was swept under different modulated magnetic field frequencies $\omega/2\pi$, from 500 Hz to 700 Hz, with a fixed modulated amplitude $B_m = 360$ nT. At each turn the first-order resonance points were recorded, as depicted in Figure 3a.

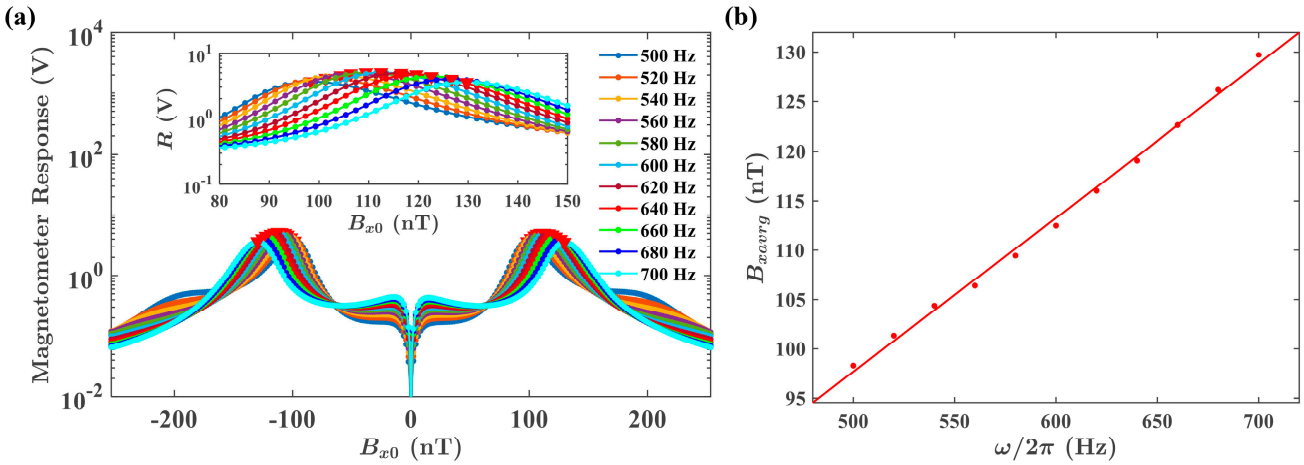

Figure 3. (**a**) Magnetometer responses when sweeping the magnetic field offset B_{x0} under different modulated magnetic field frequencies ranging from 500 Hz to 700 Hz. Each peak of R at the first-order resonance is marked with a red inverted triangle and recorded. (**b**) Each first-order resonance point B_{xavrg} (red solid circle) with different modulated magnetic frequencies $\omega/2\pi$. The fit value is presented as a red solid line.

Two first-order resonance points, corresponding to B_{x1} with $n = 1$ and B_{x-1} with $n = -1$, were extracted, averaged as B_{xavrg}, and plotted with the corresponding $\omega/2\pi$ in Figure 3b, wherein the fit value was obtained based on the proportional relationship between B_{xavrg} and $\omega/2\pi$. In addition, the derived value of $q(P)$, which is called q_{fit}, was further calculated for each fit value of B_{xavrg} (the red solid line in Figure 3b). Then, we actively employed different magnetic field offsets along the same x-axis, each corresponding to B_{xavrg}. Simultaneously, we swept $\omega/2\pi$ from 500 Hz to 700 Hz, with the same fixed modulated amplitude $B_m = 360$ nT as that used when sweeping the magnetic field offset. The magnetometer response at each sweeping turn is recorded in Figure 4a, and its peak resonant frequency $\omega_{peak}/2\pi$ is marked with red inverted triangles.

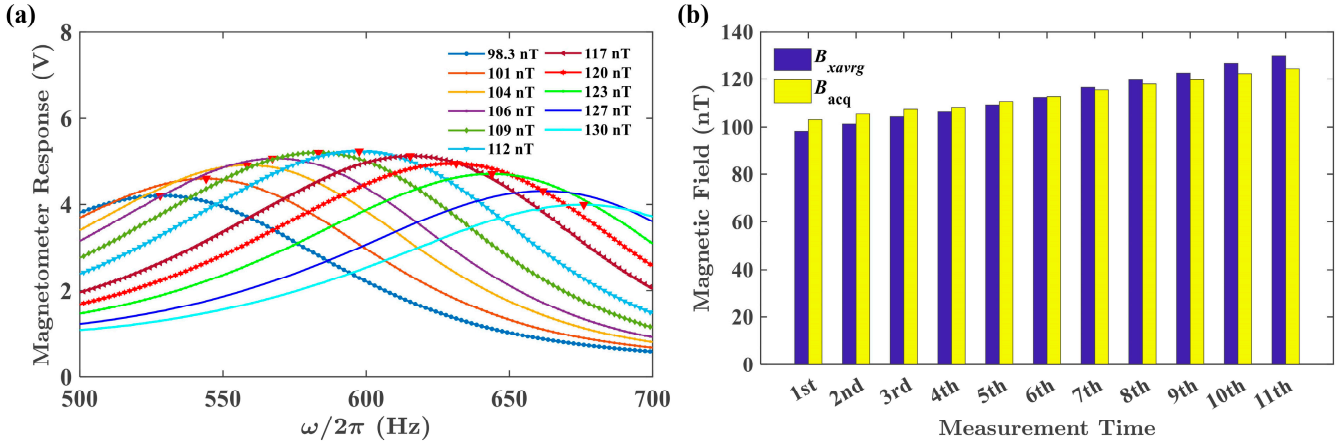

Figure 4. (**a**) Dependence of the magnetometer response on $\omega/2\pi$ under different magnetic field offsets B_{xavrg}. Resonance frequency peaks are marked with red inverted triangles. (**b**) Comparison between the active applied magnetic field B_{xavrg} and B_{acq} acquired from (**a**). The label of horizontal axis "Measurement Time" represents each measurement with different B_{xavrg}.

The measurement results for different finite field offsets are summarized in Figure 4b. The B_{acq} represents the magnetic field acquired by detecting the resonance frequency $\omega_{peak}/2\pi$, i.e., $B_{\mathrm{acq}} = q_{fit}\omega_{peak}/\gamma^e$. The label of horizontal axis "Measurement Time" represents each measurement with different B_{xavrg}, as in Figure 4a, and "1st" and "11th" correspond to "B_{xavrg}= 98.3 nT" and "B_{xavrg}= 130 nT", respectively. The B_{acq} was close to B_{xavrg}, i.e., within a 5% error range, which verified our non-zero finite measurement method based on the first-order resonance. In addition, the difference between B_{acq} and B_{xavrg} may result from the following factors: the residual magnetic field affected the detection of peaks when sweeping B_{x0} and caused the inequality between the actively applied magnetic field B_{act} and B_{xavrg}; the comprehensive effect of magnetic offset and modulated magnetic field induced the variation in the effective gyromagnetic ratio; and the nuclear slowing-down factor [30].

4.2. Spin Polarization Measurement

The spin polarization of ^{87}Rb atoms was obtained by obtaining $q(P)$, which can be measured by determining the first-order resonance point. For instance, we swept the magnetic field offset along the x-axis with different B_m values, ranging from 100 nT peak-peak value to 260 nT peak-peak value, with a $\omega_m/2\pi$ fixed at 600 Hz. The magnetometer response for each sweep is plotted in Figure 5a. The first-order resonance points were extracted and recorded, and each corresponding slowing-down factor (spin polarization) was calculated and plotted in Figure 5b to present the relationship between the slowing-down factor (spin polarization) and B_m. Increasing the modulated magnetic field amplitude B_m leads to a larger relaxation rate R_{rel}.

By utilizing the spin polarization amplitude expression in Equation (13), we determined the relationship between $q(P)$ and B_m. The R_{rel} is composed of $k_{\mathrm{SE}}\gamma_e^2 B_m^2$, related to the modulation amplitude B_m, and R_{rel2}, which is not directly related to B_m. Here, k_{SE} is the proportional factor of R_{rel} related to $\gamma_e^2 B_m^2$. For ^{87}Rb atoms, according to Equation (13), $q(P)$ can be expressed with respect to B_m as follows:

$$q(P) \propto \frac{6\left(R_{\mathrm{op}} + k_{\mathrm{SE}}\gamma_e^2 B_m^2 + R_{\mathrm{rel2}}\right)^2 + 2J_1^2(u)R_{\mathrm{op}}^2}{\left(R_{\mathrm{op}} + k_{\mathrm{SE}}\gamma_e^2 B_m^2 + R_{\mathrm{rel2}}\right)^2 + J_1^2(u)R_{\mathrm{op}}^2} \tag{14}$$

The fit of the experimental data was performed according to Equation (14), and the results indicate that the coefficient of determination r^2 of the fit is 0.993. From Figure 5b, we observed that the larger the modulated magnetic field amplitude, the lower the spin

polarization in the stable state. This finding is reasonable and consistent with the theories proposed by Shah et al. [31] and Yan et al. [32], for that the relaxation rate of alkali atoms caused by a modulated magnetic field is proportional to the squared value of the modulation amplitude.

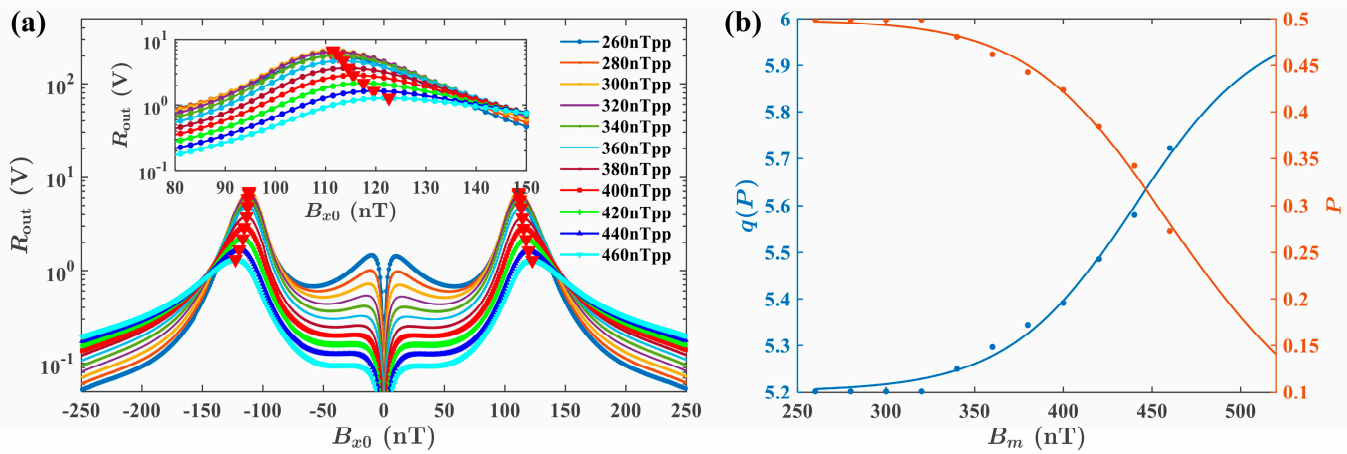

Figure 5. (**a**) Magnetometer response when sweeping the magnetic field offset along the x-axis B_{x0} with different B_m values ranging from 260 nT peak-peak value to 460 nT peak-peak value, and the $\omega_m/2\pi$ fixed at 600 Hz. The peak of each first-order resonance is marked with red inverted triangles and recorded. (**b**) The slowing-down factor $q(P)$ and spin polarization P when different B_m values are employed, wherein each record is extracted from the data depicted in subfigure (**a**). The solid circle points represent the experimental data, whereas each solid curve represents the fit curve according to Equation (14).

4.3. In Situ Coil Constant Calibration

In the experiment, the actual value we set when applying a magnetic field was voltage U_{x0}, and the coil constant along the x-axis was $k_x = B_{x0}R_x/U_{x0}$. In this equation, R_x is the known resistor value, and the certain value of B_{x0}, i.e., B_{x1}, can be acquired through the resonance condition $\gamma^e B_{x1} + q\omega_{x1} = 0$. The coil constant along the y-axis showed a similar relationship. However, simply utilizing the resonance condition to calibrate the coil constant may result in an error caused by the undetermined value of $q(P)$. Our method provides precise calibration based on combining the first-order resonance condition with the definitive value of $q(P)$ obtained by fitting.

Deriving the relationship between ω_{x1} and I_{pump} helps fitting for ω_{x1} when $I_{pump} \to 0$, i.e., $R_{\mathrm{op}} \to 0$ causes atoms unpumped with zero P and definitive $q(P) \to 6$ for ^{87}Rb atoms. At the limit of $I_{pump} \to 0$, the magnetic field at the first-order resonance is known to be $B_{x1} = 6\omega_{x1}/\gamma^e$. In this manner, the coil constants can be precisely calibrated as $k_x = B_{x1}R_x/U_{x0}$.

We swept $\omega/2\pi$, from 200 Hz to 1000 Hz, with an invariable B_{x1}. The magnetometer response is illustrated in Figure 6a. At each sweeping turn, the pump light power I_{pump} was set as a different value ranging from 0.40 mW to 2.40 mW, with a step size of 0.20 mW, and the peak of each first-order resonance is marked in Figure 6a and recorded. The other experimental parameters were consistent with simulation parameters.

Subsequently, we listed the first-order resonance points (expressed as the modulation frequency $\omega_{x1}/2\pi$), and plotted Figure 6b to denote the relationship between $\omega_{x1}/2\pi$ and I_{pump}. Determining the resonance in the modulation frequency $\omega_{x1}/2\pi$ is better than reading from the resonance when sweeping the magnetic field offset B_{x0}, due to the error caused by the residual magnetic fields.

Based on Equation (13), the relationship between $\omega_{x1}/2\pi$ and I_{pump} can be derived. R_{op} is approximately proportional to I_{pump}, and $R_{\mathrm{op}} \approx k_{\mathrm{op}} I_{pump}$. From the first-order

resonance condition $\gamma^e B_{x0} + q\omega = 0$, the proportional relationship for $\omega_{x1}/2\pi$ is $\omega_{x1}/2\pi \propto 1/q(P)$. Thereby, for ^{87}Rb atoms the expression can be derived as

$$\omega_{x1}/2\pi \propto \frac{\left(k_{\mathrm{op}} I_{pump} + R_{\mathrm{rel}}\right)^2 + J_1^2(u) k_{\mathrm{op}}^2 I_{pump}^2}{6\left(k_{\mathrm{op}} I_{pump} + R_{\mathrm{rel}}\right)^2 + 2J_1^2(u) k_{\mathrm{op}}^2 I_{pump}^2} \tag{15}$$

Equation (15) is adopted as the fit function between $\omega_{x1}/2\pi$ and I_{pump}.

We employed Equation (15) to fit the data in Figure 6b, and the fit value of ω_{x1} for $I_{pump} \to 0$ with $r^2 = 0.985$ can be obtained as $\omega_{x1\_0} = 517.0$ Hz. Consequently, we showed that $k_x = B_{x1}R_x/U_{x0}$ =14.54 nT/mA, and the coil constant along the same x-axis measured with a flux-gate magnetometer is 14.50 nT/mA, as shown in Figure 7a. This is regarded as the benchmark of the measured result of k_x herein. The coil constants k_x measured through these two methods, with a relative error of 0.29%, are almost similar. In addition, by employing a similar method, the coil constant along the y-axis was acquired as $k_y = B_{y1}R_y/U_{y0}$ =14.53 nT/mA.

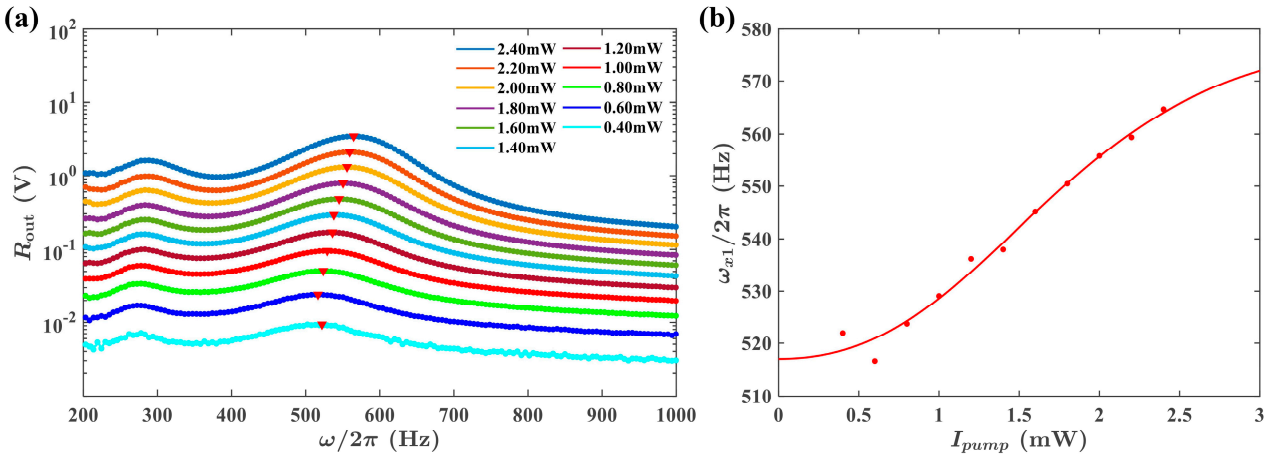

Figure 6. (**a**) Magnetometer response to different frequencies of the modulated magnetic field and with different pump light powers I_{pump} (plotted using different colors). Each peak of magnetometer response of R at the first-order resonance is marked with a red inverted triangle and recorded. (**b**) The plotted $\omega_{x1}/2\pi$ under different I_{pump}, wherein each record is extracted from the data depicted in (**a**). This plot indicates the relationship between $\omega_{x1}/2\pi$ and I_{pump}, and, moreover, the fit value of ω_{x1} for $I_{pump} \to 0$ can be acquired.

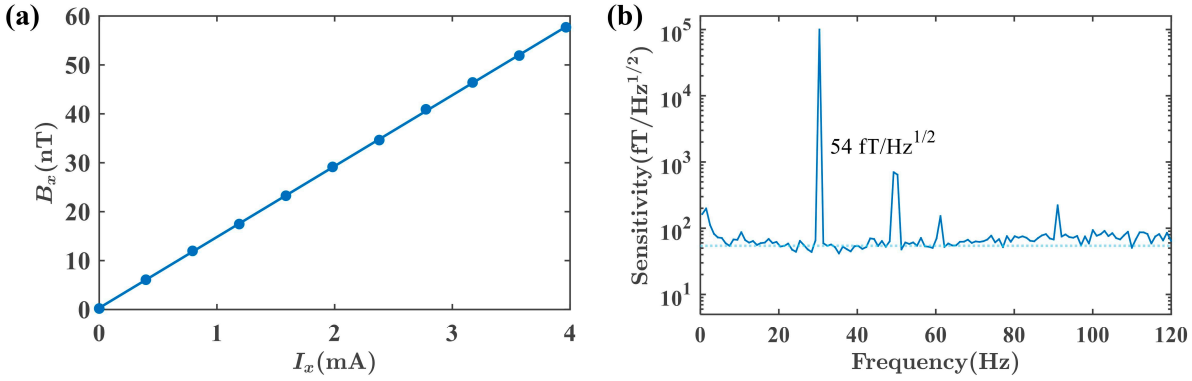

Figure 7. (**a**) The measurement of magnetic field generated by the same coil as that in Section 4.3 with different coil currents, and using a flux-gate magnetometer, for comparison. (**b**) Sensitivity of the magnetic field measurement based on the first-order resonance of single-beam SERF magnetometers. The measurement sensitivity is evaluated by applying the calibration magnetic field signal to the magnetometer along with the modulated magnetic field. The sensitivity of magnetic field measurement is 54 fT/Hz$^{1/2}$.

Furthermore, we evaluated the sensitivity of the magnetic field measurement based on the first-order resonance of a single-beam SERF magnetometer. The measurement sensitivity was analyzed by acquiring the noise spectrum of the output signal of the OPM. For direct measurement, a 100 pT_{rms} magnetic calibration signal at 30.5 Hz and the magnetic field offset corresponding to the first-order resonance pointwere employed along the sensitive axis (x-axis in the experiment). Subsequently, the voltage output signal was acquired and collected for 60 s, and a noise spectral analysis was conducted to determine the sensitivities of the magnetometer. The sensitivity results are given in Figure 7b, where the maximum peaks in each noise spectrum represent the calibration signals. The sensitivity of magnetic field measurement was 54 $fT/Hz^{1/2}$.

5. Conclusions

In this study, we assessed the nonzero-order parametric resonances of alkali-metal atoms in a single-beam SERF magnetometer and primarily focused on the first-order resonance. Based on the first-order resonance, not only can the nonzerofinite magnetic field be measured, but the spin polarization of alkali-metal atoms can also be determined by measuring the slowing-down factor. Moreover, precise calibration of the coil constants can be achieved by acquiring the first-order resonance points under a fitted equivalent zero light power (with a definitive $q(P)$ for certain types of alkali-metal atoms). Our study summarizes parametric resonance, and the proposed method has the potential to function as a component of the systematic analysis of single-beam SERF magnetometers. Future studies may focus on the comprehensive response of SERF magnetometers at different harmonic and resonance orders.

Author Contributions: Conceptualization, K.W. and K.Z.; methodology, K.W.; software, N.X.; validation, K.W., X.L. and K.Z.; formal analysis, K.W.; investigation, Y.Y.; resources, K.Z.; data curation, K.W.; writing—original draft preparation, K.W.; writing—review and editing, K.Z.; visualization, K.W.; supervision, B.Z.; project administration, K.Z.; funding acquisition, B.Z. All authors have read and agreed to the published version of the manuscript.

Funding: This study was supported by the National Natural Science Foundation of China under Grant (No. 61903013).

Institutional Review Board Statement: Not applicable.

Informed Consent Statement: Not applicable.

Data Availability Statement: The data presented in this study are available upon reasonable request from the corresponding author.

Conflicts of Interest: The authors declare no conflict of interest.

References

1. Kominis, I.K.; Kornack, T.W.; Allred, J.C.; Romalis, M.V. A subfemtotesla multichannel atomic magnetometer. *Nature* **2003**, *422*, 596–599. [CrossRef]
2. Wakai, R.T. The atomic magnetometer: A new era in biomagnetism. *AIP Conf. Proc.* **2014**, *1626*, 46–54. [CrossRef]
3. Boto, E.; Holmes, N.; Leggett, J.; Roberts, G.; Shah, V.; Meyer, S.S.; Muñoz, L.D.; Mullinger, K.J.; Tierney, T.M.; Bestmann, S.; et al. Moving magnetoencephalography towards real-world applications with a wearable system. *Nature* **2018**, *555*, 657–661. [CrossRef] [PubMed]
4. Abel, C.; Afach, S.; Ayres, N.J.; Baker, C.A.; Ban, G.; Bison, G.; Bodek, K.; Bondar, V.; Burghoff, M.; Chanel, E.; et al. Measurement of the Permanent Electric Dipole Moment of the Neutron. *Phys. Rev. Lett.* **2020**, *124*, 081803. [CrossRef]
5. Kim, Y.J.; Chu, P.-H.; Savukov, I.; Newman, S. Experimental limit on an exotic parity-odd spin- and velocity-dependent interaction using an optically polarized vapor. *Nat. Commun.* **2019**, *10*, 2245. [CrossRef] [PubMed]
6. Dang, H.B.; Maloof, A.C.; Romalis, M.V. Ultrahigh sensitivity magnetic field and magnetization measurements with an atomic magnetometer. *Appl. Phys. Lett.* **2010**, *97*, 151110. [CrossRef]
7. Higbie, J.M.; Rochester, S.M.; Patton, B.; Holzlöhner, R.; Calia, D.B.; Budker, D. Magnetometry with Mesospheric Sodium. *Proc. Nat. Acad. Sci. USA* **2011**, *108*, 3522–3525. [CrossRef]
8. Iivanainen, J.; Zetter, R.; Parkkonen, L. Potential of on-scalp MEG: Robust detection of human visual gamma-band responses. *Hum. Brain Mapp.* **2020**, *41*, 150–161. [CrossRef] [PubMed]

9. Boto, E.; Shah, V.; Hill, R.M.; Rhodes, N.; Osborne, J.; Doyle, C.; Holmes, N.; Rea, M.; Leggett, J.; Bowtell, R.; et al. Triaxial detection of the neuromagnetic field using optically-pumped magnetometry: Feasibility and application in children. *NeuroImage* **2022**, *252*, 119027. [CrossRef]
10. Li, Z.; Wakai, R.T.; Walker, T.G. Parametric modulation of an atomic magnetometer. *Appl. Phys. Lett.* **2006**, *89*, 134105. [CrossRef]
11. Hu, Y.; Hu, Z.; Liu, X.; Li, Y.; Zhang, J.; Yao, H.; Ding, M. Reduction of far off-resonance laser frequency drifts based on the second harmonic of electro-optic modulator detection in the optically pumped magnetometer. *Appl. Opt.* **2017**, *56*, 5927–5932. [CrossRef]
12. Osborne, J.; Orton, J.; Alem, O.; Shah, V. Fully integrated, standalone zero field optically pumped magnetometer for biomagnetism. In *Proceedings of the Proceedings SPIE 10548, Steep Dispersion Engineering and Opto-Atomic Precision Metrology XI*; Shahriar, S.M., Scheuer, J., Eds.; SPIE: San Francisco, CA, USA, 2018; p. 10548. [CrossRef]
13. Sheng, D.; Perry, A.R.; Krzyzewski, S.P.; Geller, S.; Kitching, J.; Knappe, S. A microfabricated optically-pumped magnetic gradiometer. *Appl. Phys. Lett.* **2017**, *110*, 031106. [CrossRef] [PubMed]
14. Wang, J.; Fan, W.; Yin, K.; Yan, Y.; Zhou, B.; Song, X. Combined effect of pump-light intensity and modulation field on the performance of optically pumped magnetometers under zero-field parametric modulation. *Phys. Rev. A* **2020**, *101*, 053427. [CrossRef]
15. Wang, K.; Zhang, K.; Zhou, B.; Lu, F.; Zhang, S.; Yan, Y.; Wang, W.; Lu, J. Triaxial closed-loop measurement based on a single-beam zero-field optically pumped magnetometer. *Front. Phys.* **2022**, *10*, 1059487. [CrossRef]
16. Cohen-Tannoudji, C.; Dupont-Roc, J.; Haroche, S.; Laloë, F. Diverses résonances de croisement de niveaux sur des atomes pompés optiquement en champ nul. I. Théorie. *Rev. Phys. Appl. (Paris)* **1970**, *5*, 95–101. [CrossRef]
17. Slocum, R.E.; Marton, B.I. Measurement of Weak Magnetic Fields Using Zero-Field Parametric Resonance in Optically Pumped He4. *IEEE Trans. Magn.* **1973**, *9*, 221–226. [CrossRef]
18. Xiao, W.; Wang, H.; Zhang, X.; Wu, Y.; Wu, T.; Chen, J.; Peng, X.; Guo, H. In Situ Calibration of Magnetic Field Coils Using Parametric Resonance in Optically-pumped Magnetometers. In Proceedings of the 2021 Joint Conference of the European Frequency and Time Forum and IEEE International Frequency Control Symposium (EFTF/IFCS), Gainesville, FL, USA, 7–17 July 2021; pp. 1–3. [CrossRef]
19. Eklund, E.J. Microgyroscope Based on Spin-Polarized Nuclei. PhD Thesis, University of California, Irvine, CA, USA, 2008.
20. Chen, C.; Jiang, Q.; Wang, Z.; Zhang, Y.; Luo, H.; Yang, K. A non-interference method for measurement of transverse relaxation time of the alkali metal magnetometer in nuclear magnetic resonance oscillator. *AIP Adv.* **2020**, *10*, 065303. [CrossRef]
21. Jiang, Q.; Luo, H.; Zhan, X.; Zhang, Y.; Yang, K.; Wang, Z. Avoiding the impact of the heater-induced longitudinal field on atomic magnetometers. *J. Appl. Phys.* **2018**, *124*, 244501. [CrossRef]
22. Yang, H.; Wang, Q.; Zhao, B.; Li, L.; Zhai, Y.; Han, B.; Tang, F. Magnetic field sensing based on multi-order resonances of atomic spins. *Opt. Express* **2022**, *30*, 6618. [CrossRef]
23. Ledbetter, M.P.; Savukov, I.M.; Acosta, V.M.; Budker, D.; Romalis, M.V. Spin-exchange-relaxation-free magnetometry with Cs vapor. *Phys. Rev. A* **2008**, *77*, 033408. [CrossRef]
24. Appelt, S.; Baranga, A.B.-A.; Erickson, C.J.; Romalis, M.V.; Young, A.R.; Happer, W. Theory of spin-exchange optical pumping of ^{3}He and ^{129}Xe. *Phys. Rev. A* **1998**, *58*, 1412–1439. [CrossRef]
25. Dong, H.F.; Fang, J.C.; Zhou, B.Q.; Tang, X.B.; Qin, J. Three-dimensional atomic magnetometry. *Eur. Phys. J. Appl. Phys.* **2012**, *57*, 21004. [CrossRef]
26. Seltzer, S.J. Developments in Alkali-Metal Atomic Magnetometry. PhD Thesis, Princeton University, Princeton, NJ, USA, 2008.
27. Chen, Y.; Zhao, L.; Zhang, N.; Yu, M.; Ma, Y.; Han, X.; Zhao, M.; Lin, Q.; Yang, P.; Jiang, Z. Single beam Cs-Ne SERF atomic magnetometer with the laser power differential method. *Opt. Express* **2022**, *30*, 16541. [CrossRef] [PubMed]
28. Wu, W.; Zhou, B.; Liu, G.; Chen, L.; Wang, J.; Fang, J. Novel nested saddle coils used in miniature atomic sensors. *AIP Adv.* **2018**, *8*, 075126. [CrossRef]
29. Wang, J.; Zhou, B.; Wu, W.; Chen, L.; Fang, J. Uniform Field Coil Design Based on the Target-Field Method in Miniature Atomic Sensors. *IEEE Sens. J.* **2019**, *19*, 2895–2901. [CrossRef]
30. Xiao, W.; Wu, T.; Peng, X.; Guo, H. Atomic spin-exchange collisions in magnetic fields. *Phys. Rev. A* **2021**, *103*, 043116. [CrossRef]
31. Shah, V.; Romalis, M.V. Spin-Exchange-Relaxation-Free Magnetometry Using Elliptically-Polarized Light. *Phys. Rev. A* **2009**, *80*, 013416. [CrossRef]
32. Yan, Y.; Lu, J.; Zhang, S.; Lu, F.; Yin, K.; Wang, K.; Zhou, B.; Liu, G. Three-axis closed-loop optically pumped magnetometer operated in the SERF regime. *Opt. Express* **2022**, *30*, 18300. [CrossRef] [PubMed]